*Solar RRL*

WILEY VCH

Solar RRL

RESEARCH ARTICLE OPEN ACCESS

# Vapor Induced Donor–Acceptor Interface to Enhance The Performance of Bilayer Organic Solar Cells

Mohamed Samir | Osbel Almora | Angel Sacramento | Josep Pallarès | Lluis F. Marsal

Department of Electronic, Electric and Automatic Engineering, Universitat Rovira i Virgili, Tarragona, Spain

**Correspondence:** Lluis F. Marsal (lluis.marsal@urv.cat)

**Received:** 3 June 2025 | **Revised:** 6 July 2025 | **Accepted:** 18 July 2025

**Funding:** Ministry of Research and Universities, Grant/Award Numbers: CESC 2023 CLIMA 00067; Spanish Ministerio de Ciencia e Innovación, Grant/Award Number: PDI2021-128342OB-I00; Agency for Management of University and Research Grants, Grant/Award Number: 2021-SGR-00739; Catalan Institution for Research and Advanced Studies

**Keywords:** bilayer organic photovoltaics | device stability | donor–acceptor interface | interface engineering | nonfullerene acceptors | vapor treatment

## ABSTRACT

In this study, we introduce the vapor-induced donor–acceptor interface (VIDAI) method to enhance the performance of bilayer organic solar cells (OSCs) through direct solvent vapor treatment at the donor–acceptor interface. Using the inverted device structure ITO/ZnO/D18/Y6/$MoO_3$/Ag, we applied 1-chloronaphthalene (CN) and 1,8-diiodooctane (DIO) vapors directly to the donor layer to treat the interface between the D18 and Y6 layers. Compared to the nontreated devices, the devices incorporating VIDAI demonstrated improvements in power conversion efficiency (PCE) under 1 sun illumination from 15.1% to 16.8% and 17.0% for CN and DIO, respectively, and for indoor illumination from 13.2% to 14.9% and 15.0% for CN and DIO, respectively. This is attributed to optimized surface tension and improved recombination lifetime. Additionally, the VIDAI method enhanced device stability, with the DIO-treated device exhibiting the highest maximum power point stability. This work establishes VIDAI as a simple, and effective, strategy for optimizing the efficiency and stability of bilayer OSCs, paving the way for their application in both outdoor and indoor energy harvesting.

## 1 | Introduction

The need for sustainable energy solutions has positioned organic solar cells (OSCs) as a promising alternative due to their lightweight, flexible, and low-cost design, along with the use of environmentally friendly materials [1]. Unlike traditional silicon-based photovoltaics, OSCs employ organic materials to enable efficient light absorption, energy conversion, and novel applications such as portable electronics and large-area roll-to-roll production [2, 3]. However, despite these promising features, OSCs still face challenges in achieving high power conversion efficiencies (PCEs) and long-term stability, primarily due to limitations in charge generation, transport, and recombination at the donor–acceptor (D–A) interface [4, 5]. Addressing these challenges through innovative interface engineering strategies is critical to achieve the full potential of OSCs for practical applications.

The D–A interface is a crucial part of OSCs, as it plays a fundamental role in exciton generation, dissociation, and charge transport. Generally, photons are absorbed at the active layer, generating excitons (bounded electron–hole pairs), which must diffuse to the D–A interface for efficient dissociation into free charge carriers [6, 7]. Optimizing the D–A interface facilitates exciton dissociation, reduces charge recombination, and enhances efficient charge extraction to the electrodes, ultimately leading to higher OSC performance [8, 9].

To overcome the challenges of the D–A interface, several strategies have been developed to improve its structural and electronic

properties. One common approach involves using solvent additives like 1,8-diiodooctane (DIO), *n*-octane, chloroform (CF) and 1-fluronaphthalene (FN) [10–13]. These additives help to adjust the phase separation and crystallinity of the active layer, consequently enhancing charge generation and transport, leading to improved overall performance. Thermal annealing (TA) is another widely used technique that refines molecular arrangement and interfacial contact between donor and acceptor materials. By applying heat, this process promotes self-organization, resulting in better alignment and improved interfacial performance [14, 15]. Moreover, incorporating interfacial layers between the active layer and the electrodes has been found to enhance charge extraction and minimize recombination losses, thereby improving the overall efficiency of the device [16, 17].

Solvent vapor treatment (SVT) has become a promising method for optimizing the D–A interface in OSCs, offering a potential way to improve performance and efficiency. SVT provides a highly controllable and direct way to optimize the morphology and electronic properties of the active layer, unlike solvent additives or TA. [12, 18–20] The SVT technique involves a way to expose the active layer to solvent vapors for a time in a sealed environment. In this case, solvent molecules diffuse into the surface of the film without fully dissolving it. [21, 22]

Solvent vapors such as chloroform (CF) and carbon disulfide ($CS_2$) offer control over the phase separation and crystallinity of the active layer, which enhances charge generation and transport [22]. Moreover, SVT can be conducted at room temperature, minimizing the risk of thermal degradation and making it suitable for flexible substrates [22].

Despite its promising potential, SVT has been underexplored in bilayer OSCs [23–25],particularly in systems that use high-performance nonfullerene acceptors like Y6 and focus on the direct interface between donor and acceptor materials. This gap in research presents an exciting opportunity to develop a scalable method with minimal thermal risk for optimizing the interface, leading to high-efficiency and stable bilayer OSCs for both outdoor and indoor applications. The simplicity of the bilayer structure compared to bulk heterojunction (BHJ) configurations [26], makes it easier to understand and control the phase separation, making it ideal for large-scale applications. We have summarized some treatment methods and their effects on bilayer systems in Table S1, Supporting Information.

Zhang et al. showed that solvent vapor annealing (SVA) with $CS_2$ in *o*-xylene-processed dual layer OSCs significantly improved the vertical distribution of components and the donor/acceptor interface, achieving a PCE value of 17.24% [22]. Moreover, the SVA-treated devices demonstrated excellent mechanical flexibility, retaining 80% of their original efficiency after 1000 bending cycles. This work highlights the potential of SVA as a powerful technique for developing high-performance, flexible OSCs.

Jiang et al. introduced a warm solution and SVA (WS + SVA) strategy to optimize the morphology of small-molecule active layers, achieving a PCE of 15.68% in all-small-molecule OSCs. This approach improved light absorption, charge generation, and extraction while enhancing film uniformity and stability. The WS + SVA method presents a promising avenue for advancing the performance and reliability of these devices [18].

Shaza et al. explored the effect of the combination of thermal and solvent annealing on D18:Y6-based OSCs. They found that annealing the active layer at 55°C with CF vapor for 5 min optimized its morphology, resulting in improved charge transfer and a PCE of 16.5% [27].

Karuthedath et al. explored the effect of adding 1-chloronaphthalene (CN) to the Y6 solution in layer-by-layer (LbL)-coated PM6/Y6 OSCs, demonstrating enhanced PCE with 0.5% CN due to improved morphology and charge dynamics. Their findings showed that optimal CN content led to LbL device performance comparable to BHs, while excessive CN (1.5%) increased film crystallinity and recombination losses [28].

Andreas et al. investigated the effect of increasing DIO content in PBDTTT-C:$PC_{71}BM$ blends and showed that the introduction of a small amount of DIO (0.6%) leads to a reduction in $PC_{71}BM$ domain size, resulting in an improvement in PCE [29].

Sooncheol et al. investigated the molecular packing behavior in P1:$PC_{71}BM$ BHs using real-time GIWAXS to reveal the impact of 1-chloronaphthalene (1-CN) as a processing additive in CB and DCB solvents. They found that 1-CN suppressed the formation of bimolecular crystals and promoted a bicontinuous interpenetrating network with improved π–π stacking, leading to a more balanced charge carrier transport. [30] Similarly, Shilong et al. introduced DIO as a processing additive in D18:Y6 OSCs and achieved a power conversion efficiency (PCE) of 17.56% [31].

In our work, we introduce a direct approach to treat the D–A interface in bilayer OSCs termed vapor-induced donor–acceptor interface (VIDAI). This method involves treating donor layer with solvent vapor before depositing the acceptor layer. We have applied the VIDAI approach to nonfullerene acceptor-based OSCs with an inverted device structure: indium tin oxide (ITO) as transparent electrode, zinc oxide (ZnO) as electron-transport layer (ETL), D18 polymer as donor layer, Y6 as acceptor layer, molybdenum trioxide ($MoO_3$) as hole-transport layer (HTL), and silver (Ag) as the back electrode (see Figure 1a). D18 donor layer was exposed to solvent vapors 1-chloronaphthalene (CN) and 1,8-diiodooctane (DIO) for 10 min, followed by the deposition of the Y6 acceptor layer (see Figure 1b). This treatment directly modifies the interface between D18 and Y6, enhancing its electronic and donor surface properties. To evaluate the effectiveness of VIDAI, we fabricated and compared three types of devices: a "Control" device without any treatment, a "CN-treated" device exposed to 1-chloronaphthalene vapor, and a "DIO-treated" device exposed to 1,8-diiodooctane vapor (see Table S2). This systematic study aims to demonstrate the potential of VIDAI as a scalable and effective strategy for improving the performance of bilayer OSCs avoiding the risk of TA between the donor and acceptor layer.

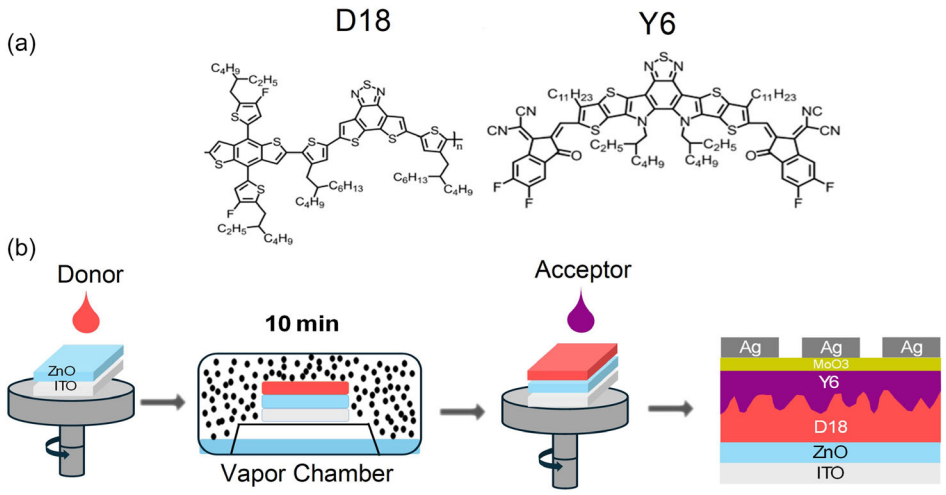


**FIGURE 1** | (a) Molecular structures of D18 and Y6 that used in the solar device (ITO/ZnO/D18/Y6/$MoO_3$/Ag). The literature values used for the energy positions in the energy diagram are summarized in Table S3 (Supporting Information). (b) Schematic illustration of the vapor treatment method (VIDAI) used in the fabrication process.

## 2 | Results and Discussion

### 2.1 | Device Characteristics

The structure ITO/ZnO/D18/Y6/$MoO_3$/Ag for the three devices: Control, DIO, and CN has been studied using the current density–voltage ($J$–$V$) characteristics under 1 sun illumination as shown in Figure 2a. The extracted parameters from the $J$–$V$ curve are summarized in Table S4 with statistics in Figure S1. The Control device exhibits a PCE of 14.4%, with a maximum PCE of 15.1%, an average short-circuit current density ($J_{sc}$) of 25.1 mA/cm$^2$, a fill factor (FF) of 70%, and an open-circuit voltage ($V_{oc}$) of 0.84 V. In contrast, the DIO-treated device demonstrates the highest $J_{sc}$ of 27.0 mA/cm$^2$, an FF of 73%, $V_{oc}$ of 0.85 V, achieving an average PCE of 16.1%, and a maximum PCE of 17.0%. This indicates significant improvements in charge carrier generation and extraction compared to the Control device.

The CN-treated device also shows a moderate enhancement, with a $J_{sc}$ of 26.4 mA/cm$^2$ and an FF of 73%, similar to the DIO-treated

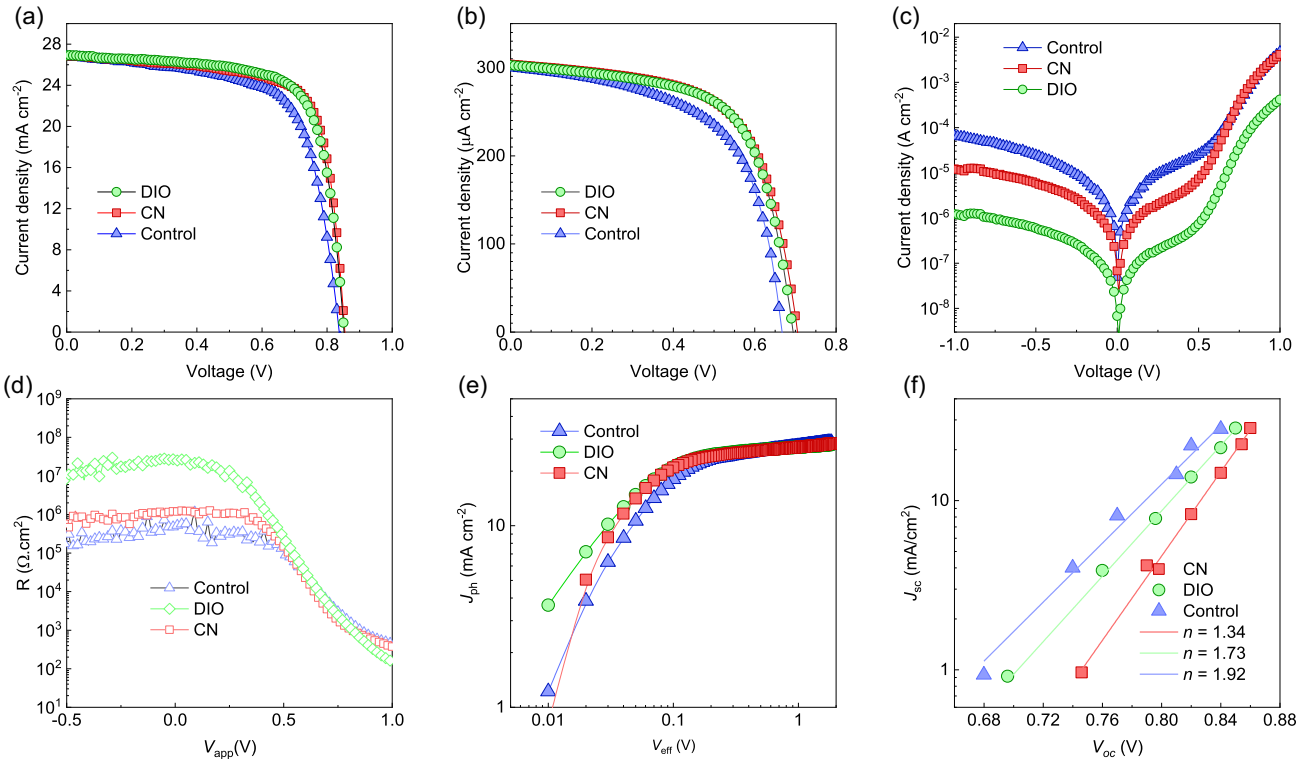


**FIGURE 2** | (a) Current density–voltage ($J$–$V$) curve of the device under 1 sun illumination. (b) $J$–$V$ curve under indoor illumination (2500lx). (c) $J$–$V$ curve measured in the dark. (d) The dark DC resistances. (e) $J_{ph}$ versus $V_{eff}$. (f) Short-circuit current versus open-circuit voltage for different illumination intensities.

device. This suggests that the SVT with 1-chloronaphthalene (CN) positively impacts the donor (D18)–acceptor (Y6) interface as well. Additionally, the CN-treated device exhibits a $V_{oc}$ of 0.86 V, an average PCE of 16.1%, and a maximum PCE of 16.7%. The $V_{oc}$ remains relatively consistent across all devices, indicating that the VIDAI treatment primarily enhances interfacial properties without significantly altering the energy level alignment.

In addition to testing under standard 1 sun (simulated outdoor) illumination, we exposed the fabricated devices to indoor lighting conditions. We conducted *J–V* measurements under 2500 lx light-emitting diode (LED) indoor illumination as illustrated in Figure 2b where the spectrum of the LED is shown in Figure S2. The 2500 lx luminance was chosen as it falls within the range of standard indoor illumination levels encountered in residential, office, and commercial environments [32, 33]. The *J–V* curves parameters under indoor illumination indicate notable performance trends for the Control, CN-treated, and DIO-treated devices, as summarized in Table S5 and its statistics in Figure S3. Under indoor conditions and an incident power of 900 microW/cm$^2$, the Control device exhibits a $V_{oc}$ of 0.67 V, a $J_{sc}$ of 300.2 μA/cm$^2$, an FF of 59%, and a PCE of 13.2%. The CN-treated device shows improved performance, with a $V_{oc}$ of 0.71 V, a $J_{sc}$ of 303. 9 μA/cm$^2$, an FF of 62%, and a PCE of 14.9%. Similarly, the DIO-treated device achieves a $V_{oc}$ of 0.70 V, a $J_{sc}$ of 302.8 μA/cm$^2$, an FF of 64%, and a PCE of 15.0%.

These results indicate that the VIDAI treatment enhances device performance under both 1 sun and indoor illumination. Under 1 sun illumination, the DIO-treated device demonstrates the highest $J_{sc}$ and FF, leading to superior PCE, while the CN-treated device also shows significant improvements compared to the Control. Under indoor illumination, both the CN- and DIO-treated devices exhibit higher $V_{oc}$, $J_{sc}$, and FF values, resulting in enhanced PCE values compared to the Control. This consistency in performance improvement across different lighting conditions underscores the effectiveness of the VIDAI approach in optimizing the D–A interface for diverse operational environments.

Figure 2c illustrates the dark *J–V* curves for the devices to analyze their diode characteristics, recombination processes, and leakage currents in the absence of illumination. The dark DC resistance–voltage (*R–V*) curve in Figure 2d was derived from the dark *J–V* characteristics according to the differential Equation S13 [34] (Supporting Information).

In the reverse bias region (−1 to 0 V), the current density represents leakage currents [35]. The DIO-treated device demonstrates the lowest leakage current, followed by the CN-treated device, while the Control device exhibits the highest leakage. The results show a noticeable increase in shunt resistance ($R_{sh}$) for the DIO-treated device compared to the other devices. In the reverse bias region, the difference in $R_{sh}$ between the devices is particularly clear. The Control device shows the lowest $R_{sh}$ in the reverse and forward bias which suggests that the VIDAI effectively minimizes leakage currents and improves charge collection efficiency.

We highlight that the DIO-treated device achieves the best diode characteristics, with lower recombination losses and leakage currents, further supporting the effectiveness of the VIDAI approach in optimizing the D–A interface which could be the reason to the highest short current density of DIO as shown in Figure 2a.

To check the effect of the VIDAI on different bilayer structures, we have used the same donor (D18) and acceptor (Y6) to fabricate a conventional bilayer structure of ITO/PEDOT:PSS/D18/Y6/PDINO/Ag as illustrated in Figure S4a (Supporting Information). The *J–V* curves under 1 sun illumination for the conventional structure devices in Figure S4b (Supporting Information) illustrate the universality of the VIDAI treatment. The Control device shows a $V_{oc}$ of 0.80 V, a $J_{sc}$ of 27.3 mA/cm$^2$, an FF of 63%, and a maximum PCE of 13.9%. In comparison, the CN-treated device shows improved performance, with a $V_{oc}$ of 0.82 V, a $J_{sc}$ of 27.3 mA/cm$^2$, an FF of 68%, and a maximum PCE of 15.4%. Similarly, the DIO-treated device achieves a $V_{oc}$ of 0.82 V, a $J_{sc}$ of 27.4 mA/cm$^2$, an FF of 68%, and a maximum PCE of 15.6% (see Table S6).

These findings show that the VIDAI treatment improves device performance in both inverted and conventional structures, demonstrating its broad applicability. Both CN- and DIO-treated devices achieve higher FF and PCE values than the Control, indicating that SVT enhances the D–A interface for better charge extraction and reduced recombination. However, the conventional device structure shows slightly higher short-circuit current densities, likely due to optical interference effects, the inverted devices consistently deliver higher open-circuit voltages and FFs. This suggests that the inverted configuration benefits from reduced recombination losses, potentially due to a more favorable interfacial morphology and a stronger built-in electric field, factors further enhanced by the VIDAI treatment.

Additionally, intermixing at the D–A interface, especially after TA, can induce self-segregating of Y6 toward the ZnO interface. This redistribution can enhance electron transport via formation of ordered crystalline domains and self-assembled pathways within the blend. Compared to a conventional architecture, where the donor lies below the acceptor and transport layers are in their typical positions, inverted devices can still achieve comparable or superior performance [36, 37].

Figure 2e shows photocurrent density ($J_{ph}$) as a function of the effective voltage ($V_{eff}$) [38] for the three devices. This plot has been extracted from the illuminated and dark *J–V* curves. In Section S3.1 (Supporting Information), we show the theoretical background for the photocurrent density versus the effective voltage, and we summarized in Table S7 (Supporting Information) the extracted parameters of the saturation current density ($J_{sat}$), maximum exciton generation rate ($G_{max}$), generation rate ($G$), and exciton dissociation probabilities ($P_{diss}$). Figure S5 (Supporting Information) shows the theoretical $J_{ph}$, $J_L$, and $J_D$ as a function of voltage.

At low $V_{eff}$, $J_{ph}$ increases linearly with voltage, indicating efficient charge carrier generation and extraction. As $V_{eff}$ increases, $J_{ph}$ stabilizes, signifying the saturation regime where the electric field is sufficiently high to dissociate all photogenerated excitons. The saturation current density ($J_{sat}$) and $P_{diss}$ are critical parameters for evaluating device performance. We can see that the $J_{ph}$ of Control device starts to stabilize at $V_{eff} > 0.14$ V while for the treated devices of DIO and CN it starts to stabilize for $V_{eff} < 0.14$ V, which favors charge carrier separation at low effective voltage [39].

For the Control device, $J_{sat}$ is 27.2 mA/cm$^2$, $P_{diss}$ is 92%, $G_{max}$ is $7.2 \times 10^{25}$ cm$^{-3}$s$^{-1}$, and $G$ is $6.6 \times 10^{25}$ cm$^{-3}$s$^{-1}$. The CN-treated device shows a $J_{sat}$ of 27.1 mA/cm$^2$, a $P_{diss}$ of 98%, a $G_{max}$ of $7.6 \times 10^{25}$ cm$^{-3}$s$^{-1}$, and a $G$ of $7.4 \times 10^{25}$ cm$^{-3}$s$^{-1}$. The DIO-treated device exhibits a $J_{sat}$ of 27.1 mA/cm$^2$, a $P_{diss}$ of 99%, a $G_{max}$ of $7.8 \times 10^{25}$ cm$^{-3}$s$^{-1}$, and $G$ of $7.7 \times 10^{25}$ cm$^{-3}$s$^{-1}$. These results indicate that both the CN and DIO treatments significantly enhance exciton dissociation and charge carrier generation compared to the Control device. The higher $P_{diss}$ values for the CN- and DIO-treated devices indicate an efficient exciton dissociation process at the tripling interface of the donor (D18) and acceptor (Y6) [40]. This finding aligns with the highest FF observed for the treated devices, as shown in Table S4 and S6. The increased $G_{max}$ and $G$ values suggest that the treatments enhance the overall photon-to-charge carrier conversion efficiency and more light harvesting [35, 41].

We investigated charge carriers recombination in the fabricated devices by examining their photocurrent density–photovoltage ($J_{sc}$–$V_{oc}$) behavior under different light intensities, as illustrated in Figure 2f, to evaluate the ideality factor ($n$), a parameter that indicates whether recombination occurs through radiative or nonradiative mechanisms [34]. The ideality factor is a critical parameter for understanding the nature of recombination within the devices; more details are given in Section S3.2 and Figure S6 (Supporting Information).

We summarized the ideality factor of the fabricated devices in Table S8 (Supporting Information). The Control device exhibits the highest ideality factor ($n = 1.92$), which can be associated with significant trap-assisted recombination and nonradiative losses. This suggests that the Control device suffers from more defects and inefficient charge carrier extraction compared to the treated devices. The CN-treated device shows a lower ideality factor ($n = 1.34$) in comparison with DIO ($n = 1.73$) which is closer to the ideal value of 1. This reduction in $n$ suggests that the CN treatment effectively reduces trap-assisted recombination, improving charge carrier transport and extraction [42, 43]. The lower ideality factor could also be associated with improved interfacial properties and fewer defects in the CN-treated device.

The external quantum efficiency (EQE) shown in Figure 3a was measured for the fabricated devices: DIO, CN, and the Control device. The integrated current densities (under AM1.5G spectrum) and bandgaps (from the inflection points) were extracted from the EQE spectra and are summarized in Table S9 [44]. The Control, CN-, and DIO-treated devices exhibit integrated current densities of 25.5, 26.8, and 26.9 mA/cm$^2$, respectively. The three samples also show the same photovoltaic bandgap of 1.37 eV.

This consistency suggests that the VIDAI treatment enhances the overall light absorption and charge carrier generation, contributing to the higher performance of the treated devices. The bandgap remains consistent across all devices, indicating that the VIDAI treatment does not significantly alter the optical properties of the active layer. Instead, the improvements in EQE and integrated current density are likely due to enhanced charge carrier extraction and reduced recombination losses, as evidenced by the lower ideality factors and higher $P_{diss}$ observed in Table S7 and S8.

Figure 3b shows the absorbance of the active bilayer D18/Y6 that deposited on ITO for the Control, DIO, CN devices; in addition, we include the absorbance of D18 only to detect which peak belongs to the donor (D18). As illustrated in Figure 3b, the absorbance spectra of the active bilayer D18/Y6, processed with varying treatment, exhibit a broad absorption range from 400 to 900 nm, characteristic of D18/Y6 molecules. The absorbance spectrum of the D18 layer alone shows a primary absorption peak in the range of 400–600 nm, which is characteristic of the donor material. This peak corresponds to the π–π* transition in the conjugated polymer, indicating strong light absorption in the visible region. [12, 45] The absorbance spectrum of the Control device (D18/Y6 bilayer) exhibits a broader absorption range compared to the D18 layer alone, extending into the near-infrared region (up to ~900 nm). This broadening is attributed to the contribution of the Y6 acceptor, which absorbs strongly in the longer wavelength region [45].

The CN- and DIO-treated devices show a similar absorption profile to the Control device but with a clearly enhanced absorbance in the 600–900 nm range. This improvement aligns with the higher EQE, and integrated current density observed for the CN-treated device, suggesting that the CN treatment enhances the light-harvesting efficiency of the active layer, particularly in the near-infrared region.

To provide insights into the exciton dynamics and recombination processes in these devices, photoluminescence (PL) spectra of

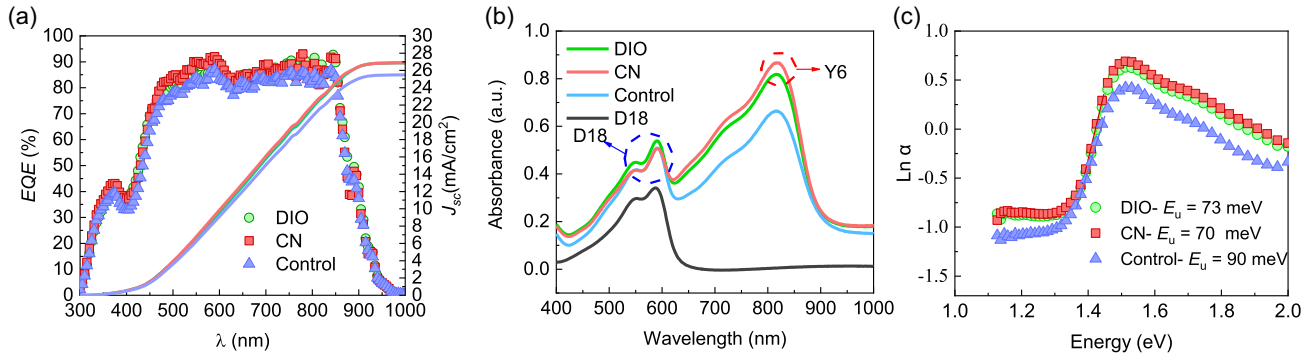


**FIGURE 3** | (a) External quantum efficiency. (b) Absorbance of the bilayer D18/Y6 on ITO substrate after deposition of the absorber layer on ITO. (c) The logarithm of the absorption coefficient versus the photon energy for estimation of the Urbach energies.

bilayer D18/Y6 without treatment and with treatments of DIO and CN were measured as illustrated in Figure S7. The D18/Y6 films were deposited onto glass and have been excited at a wavelength of 550 nm. The deposited film of the Control device shows the highest PL emission intensity in a comparison with the films of the DIO and CN devices. The film of the CN-treated device shows the lowest PL emission intensity or the highest quenching among the three devices.

We can observe that the CN-treated device shows the highest absorbance in the 600–800 nm region of the absorbance spectrum as shown in Figure S7 and the highest quenching in the PL emission intensity suggests a strong correlation between light absorption and exciton dissociation efficiency. The enhanced absorbance indicates that more photons are absorbed in this region, leading to higher exciton generation. The low PL intensity indicates that these excitons are efficiently dissociated into free charge carriers rather than recombining radiatively. This efficient exciton dissociation is likely due to the improved D–A interface achieved through the CN treatment, which facilitates charge separation and reduces recombination losses. In addition, the PL spectra of the treated films could be an indication for the good interdiffusion of the acceptor Y6 into the donor layer D18 where it forms a structure similar to that of the D18:Y6 bulk film. This bilayer interdiffusion could provide a prevalent donor/acceptor interface within the active layer [46].

Figure 3c illustrates the absorption coefficient ($\alpha$) versus the energy photon ($h\nu$) that have been extracted from Figure 3b to calculate the Urbach energy ($E_u$) using the following equation [47]

$$\alpha = \alpha_0 \exp\left(\frac{h\nu}{E_u}\right) \tag{1}$$

where $\alpha_0$ is the constant and $h\nu$ is the photons energy. The $E_u$ values extracted from the UV absorbance data provide insights into the disorder and defect states within the active layers of the Control, CN-treated, and DIO-treated devices [47, 48], where the Urbach energy of the devices was defined with the absorption tail or Urbach tail which is shown in Figure 3c is below 1.5 eV [49]. The CN-treated device shows a lower $E_u$ value of 70 meV with a closer value of DIO with $E_u$ of 73 meV, suggesting a more ordered structure with fewer defects, contributing to improved charge transport and reduced recombination. These results can be attributed to a reduction in structural disorder and defect states within the active bilayer (D18/Y6) as a result of the direct vapor treatment, which, in turn, enhances its optical properties [50].

Impedance spectroscopy (IS) has been measured to investigate the impact of the VIDAI approach on the performance of the fabricated bilayer OSCs. This technique is a powerful diagnostic method for analyzing recombination, carrier accumulation, and transport behavior within each layer of the OSCs [51–54].

Figure 4a illustrates the IS spectra in Nyquist plot representation for a single illumination intensity and the equivalent circuit employed for the analytical modeling of impedance spectra is illustrated inset. Under illumination, Figure S9 shows a set of arcs in Nyquist representation for different voltage conditions, where the recombination resistance is significantly larger for the DIO sample than those of the CN and Control devices. The spectra were fitted to the equivalent circuit model, and the recombination lifetime and resistance results are shown in Figure 4b,c, respectively. A higher recombination lifetime has been observed for the DIO and CN devices compared to the Control device, suggesting the effectiveness of the VIDAI method in improving interfacial charge transfer. Figure 4d illustrates the MS plot, which represents the dark capacitance as a function of direct current (DC) mode bias at frequency of 1 kHz and allows estimation of the built-in potential ($V_{bi}$), doping density, and charge carrier distribution within the devices. Particularly, the $V_{bi}$ is easily found from the plot intercept with the abscissa axis and the charge carrier or doping density is typically extracted from the one-sided abrupt junction approximation [55]:

$$C = \sqrt{\frac{q\epsilon\epsilon_0 N}{2(V_{bi} - V)}} \tag{2}$$

where $N$ is the doping density, $C$ is the capacitance, $q$ is the elementary charge, $\epsilon_0$ is the vacuum permittivity, $\epsilon$ is the dielectric constant, $V_{bi}$ is the built-in voltage, and $V$ is the applied bias [55, 56]. The extracted parameters are summarized in Table S12. The estimated values for $V_{bi}$ are 0.66, 0.72, and 0.75 V for the Control, CN, and DIO devices respectively. We noticed that the treated devices of CN and DIO have higher $V_{bi}$ values compared to the Control one where this increased $V_{bi}$ may facilitate charge collection, minimizing interfacial recombination and consequently improving device performance [53, 57, 58].

A detailed microscopic analysis was conducted using atomic force microscopy (AFM) to examine the morphological variations in the donor layer induced by the VIDAI approach. The morphology of the D18 film deposited on the ITO layer was characterized under three conditions: without treatment (Control device), with CN treatment, and with DIO treatment. This investigation aimed to interpret the influence of these treatments on the structural properties of the donor layer.

Figure 5a illustrates the AFM topography image of the D18 film for the DIO device, while the topography of DIO, CN, and Control devices of the blend films and D18 film for these devices are provided in Figure S10 (Supporting Information). Table S12 summarizes the results from the AFM morphology. The root mean square (RMS) roughness of the D18 film values are 1.94 nm for Control device, 1.46 nm for the DIO-treated device, and 1.22 nm for the CN-treated device, while the RMS of the active layer (D18/Y6) values are 1.45 nm for Control device, 1.44 nm for the DIO-treated device, and 1.41 nm for the CN-treated device. These results indicate that the CN treatment results in the smoothest surface, followed by the DIO-treated device, while the Control device exhibits the highest surface roughness. This observation could be attributed to a reduction in domain size [59].

The CN-treated film exhibited a smoother surface, which likely facilitated the interdiffusion of the acceptor layer into the donor layer. This interaction resulted in larger domain sizes, influencing the UV absorbance spectrum, as shown in Figure 3b, where the Y6 peak was the highest in the case of CN treatment,

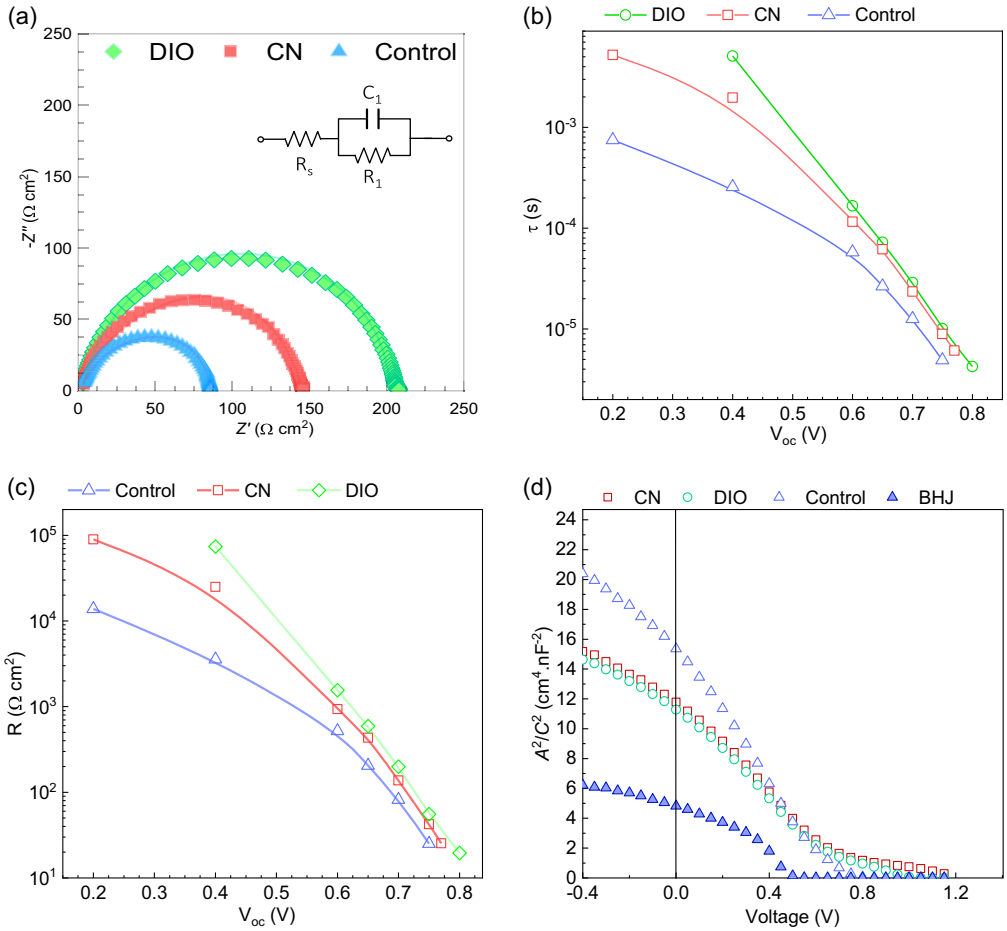


**FIGURE 4** | (a) Illustrative impedance spectroscopy spectra in Nyquist plot representation for a single illumination intensity. (b) Characteristic response/recombination lifetime as a function of open-circuit voltage. (c) Resultant resistance from the equivalent circuit model fitting of Nyquist plot. See Section S3.4 and Figure S8 for full data and further model details. (d) Dark capacitance as a function of DC bias in Mott–Schottky (MS) representation.

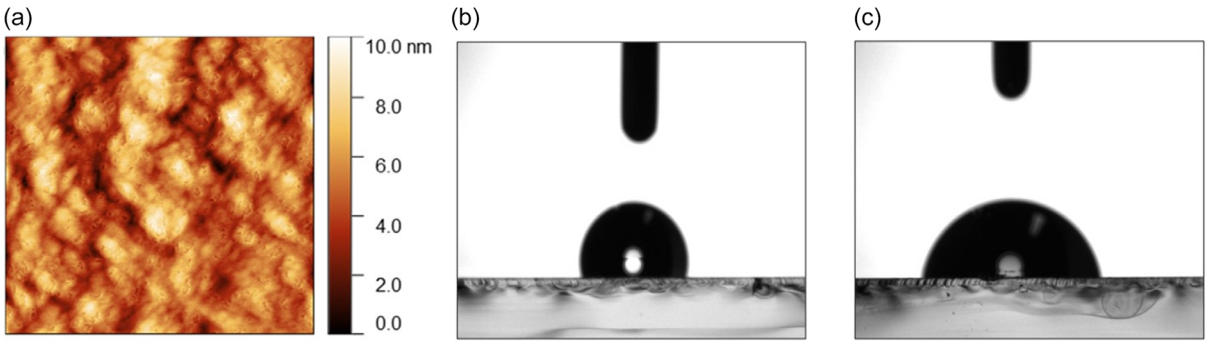


**FIGURE 5** | (a) AFM topography of the donor layer D18 for DIO on an ITO substrate. Contact angle for a drop of (b) water and (c) ethylene glycol (EG) on the donor layer D18 of DIO.

indicating enhanced crystallinity of the active layer and improved structural organization [21].

The smoother donor surface induced by CN vapor treatment reduces surface roughness and minimizes domain wall pinning, thereby facilitating more efficient domain growth and phase separation during film formation. This improved morphology promotes interdiffusion of Y6 into the donor layer and enhances molecular self-organization, leading to larger, more crystalline domains. The resulting increase in π–π stacking, particularly in Y6, contributes to the intensified UV absorbance observed, indicating improved structural ordering and optical properties of the active layer [60, 61].

The enhanced UV–vis absorption and higher FF observed in the VIDAI can be attributed to the increased aggregation of Y6 where larger domain sizes create more efficient pathways for charge transport while simultaneously reducing charge recombination [21, 62].

DIO exhibits a less smooth surface compared to CN but demonstrates improved miscibility, as evident from the phase images. The use of 1,8-diiodooctane (DIO) as an additive has been widely reported to enhance device performance by promoting a more ordered active layer with increased crystallinity [55]. This higher degree of order facilitates better nanoscale phase separation, ultimately improving charge transport and collection. Consequently, the DIO-treated device achieves enhanced $J_{sc}$ and FF, contributing to superior overall performance.

The contact angles of water ($H_2O$) and ethylene glycol (EG), along with the derived surface tension (ST) and Flory–Huggins interaction parameters ($X^{D-A}$), reveal important trends in the wetting behavior and interfacial interactions at the D–A interface, both with and without SVT. Figure 5b,c shows the contact angle of a drop of $H_2O$ and a drop of EG, respectively, on the D18 layer of DIO. Additionally, we present the contact angle of a drop of $H_2O$ and a drop of EG for the Y6 beside to the CN and Control devices in Figure S10c, which aids in determining the surface tension and the Flory–Huggins interaction parameter to assess the compatibility between the donor and acceptor layers.

Surface tension determines how well one material wets or adheres to another. Higher surface tension generally leads to better wettability, which improves interfacial contact and enhances efficient charge transfer between the donor and acceptor layers. A well-matched surface tension between the donor and acceptor layers facilitates optimal nanoscale phase separation, which is crucial for efficient exciton dissociation and charge transport [45, 63].

Section S3.6 (Supporting Information) explains the theoretical background of measuring the energy tension and Flory–Huggins parameters using Wu method as well as the results are summarized Table 1. The surface tensions were determined by Wu's method to be 61.9, 63.2, 62.8, and 63.02 mN/m for Control, CN, DIO, and Y6 films, respectively. The Flory–Huggins parameters between donor and acceptor layers ($\chi$) are accordingly estimated to be 0.005, 0.0001, and 0.0001 mN/m for Control, CN, and DIO films.

**TABLE 1** | Summary of the results from the contact angle measurements in Figure 5 and Figure S10.

| Sample | $H_2O$ [∈] | EG [∈] | Surface tension (mN/m) | $\chi_{D-A}$ [mN/m] |
|---|---|---|---|---|
| Control | 105.3 | 77.3 | 61.9 | 0.0050 |
| CN | 103.2 | 80.4 | 63.2 | 0.0001 |
| DIO | 104.4 | 80.0 | 62.8 | 0.0001 |
| Y6 | 105.6 | 78.8 | 63.0 | – |

In addition, Figure S10d shows the morphology of the Field emission scanning electron microscopy (FESEM) images of the D18/Y6 active layers deposited on ITO for Control, CN-treated, and DIO-treated films. These images show a slight difference between the treated films and the control film. The control film exhibits a relatively uniform but slightly rougher surface. In contrast, the CN- and DIO-treated films show a more uniform coverage for the ITO and smoother texture, consistent with reduced surface roughness.

The CN-treated donor layer has the highest surface tension (63.2 mN/m) which is closer to the one of the DIO-treated film, indicating better wettability and interfacial compatibility with the acceptor (Y6). This correlates with its smoother surface morphology and enhanced charge transport properties. Moreover, the CN- and DIO-treated devices both have very low $\chi$ values (0.0001 mN/m), indicating excellent miscibility between the donor (D18) and acceptor (Y6).

Although the possibility of partial swelling or limited dissolution of the underlying treated interface of D18 layer during Y6 deposition, the Flory–Huggins interaction parameters ($\chi$) confirm that having vapor additive treatment prior to acceptor deposition can significantly influence interfacial morphology and support more efficient charge generation and transport in the final device. This conclusion is further supported by the UV–vis absorption spectra as shown in Figure 3b, which show an unchanged D18 peak, implying minimal disruption to the donor film, and an enhanced Y6 signal, referring to improved acceptor packing or interfacial accumulation. Together, these findings suggest that any potential swelling does not compromise the integrity or functionality of the D18 layer but may actually contribute to favorable intermixing at the interface.

## 2.2 | Stability Study

To evaluate the stability of the fabricated OSCs with and without VIDAI treatment, we performed tests under different conditions, detailed in Table S13 (Supporting Information). These tests included maximum power point (MPP) tracking and light soaking under indoor illumination. The resulting data were compared with previously reported stability results for D18:Y6 devices under similar conditions, as summarized in Table S14 (Supporting Information). This comparison highlights the impact of the VIDAI treatment on improving the long-term stability of the OSCs.

We have tracked the MPP under constant illumination by exposing the fabricated devices to operational conditions simulating real-world use: a nonisolated holder with continuous MPP tracking under 1 sun equivalent white LED illumination at air atmosphere of temperature 333–343K and humidity of 60±5% with spectrum shown in Figure S11 (Supporting Information). Figure S12a illustrates the test workflow for MPP. The MPP tracking consists of applying the voltage corresponding to the MPP with systematic corrections accounting for the stability of the sample and the normalized MPP is shown in Figure 6a.

The Control device shows a rapid decline reaching 80% of its initial MPP after ≈3.8 h while the bilayer device with CN vapor treatment reached 80% of its initial MPP after ≈7.2 h. The highest stability has been exhibited by the bilayer device with DIO vapor treatment where it is 80% of its initial MPP after ≈12.5 h.

Figure S13 illustrates the effect of VIDAI treatment on the stability of the fabricated devices under continuous indoor illumination (see the workflow chart in Figure S12b, Supporting Information). Figure S13a, b, c, and d presents the normalized PCE, $J_{sc}$, FF, $V_{oc}$, respectively, over time. Figure 6b shows the $J$–$V$ curves for both fresh and aged devices under indoor

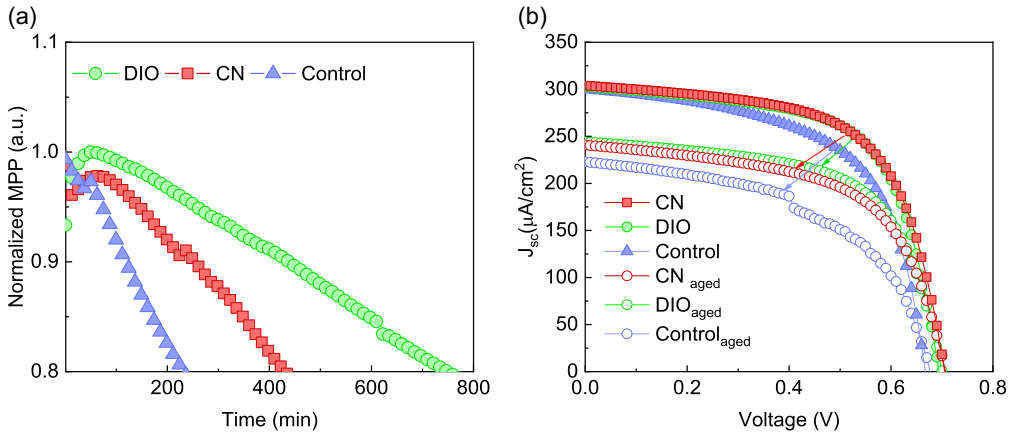


**FIGURE 6** | Device stability tests considering (a) operation under room conditions with MPP tracking under continuous 1 sun illumination (LED equivalent) and (b) *J*–*V* curves before and after the degradation test under 2500 lx illumination and open-circuit conditions. In all cases, the samples were unencapsulated at room temperature (~25°C) and with relative humidity ~ 60%.

illumination. The stability test results can be further evaluated by analyzing degradation rates (DRs), which provide a quantitative assessment of performance deterioration over time [64]. TheDR is calculated as the difference in a performance parameter (such as PCE or MPP) between the initial and final states, divided by the test duration, as expressed by the equation

$$\mathrm{DR} = \frac{X_{\mathrm{final}} - X_{\mathrm{initial}}}{t_{\mathrm{st}}} \tag{3}$$

where $t_{st}$ is the stability test of duration. Using the data from MPP stability, the DRs are −0.006, −0.02, −0.04 mW/h for DIO, CN and Control devices, respectively. Moreover, for the open-circuit stability test under 2500lx indoor conditions in Figure 6b, the resulting DRs were −0.007, −0.009, and −0.011 μW/h for DIO, CN, and Control devices, respectively. In all cases, the VIDAI-treated devices demonstrate significantly better stability compared to the Control devices.

Both CN and DIO treatments optimize the D–A interface, as evidenced by the smoother surface morphology and lower Flory–Huggins interaction parameter. This reduces defect states and recombination losses, which are primary contributors to device degradation. The use of DIO vapor appears to enhances both the performance and stability of the devices by preventing undesirable morphological changes where DIO has the ability to hinder the formation of shallow trap levels in the bandgap (self-doping), which can alter the intrinsic properties of the absorber layer as has been reported [55].

In addition, the DIO treatment has been reported to enhance the dielectric constant of the active layer by promoting a more ordered and well-mixed blend morphology. This improved morphology reduces the distance between donor and acceptor domains, facilitating better charge separation and reducing recombination losses [65]. A higher dielectric constant in the active layer can lead to better screening of Coulombic interactions between charge carriers, reducing the likelihood of charge trapping and recombination [66]. This suppression of recombination losses directly contributes to the enhanced stability of the DIO-treated device, as observed in our stability measurements (745 min to reach 80% of initial MPP).

Moreover, the stability observed during MPP tracking can be attributed to the phase separation between donor and acceptor domains within the material. This separation enhances charge carrier collection at the electrodes. These results highlight the potential of the VIDAI approach, especially with DIO, for developing stable and efficient OSCs [67].

## 3 | Conclusions

In conclusion, this study introduces the VIDAI approach for direct treatment in bilayer OSCs to control the donor/acceptor interface. Treating the donor layer (D18) with 1-chloronaphthalene (CN) and 1,8-diiodooctane (DIO) vapors before depositing the acceptor (Y6) improved interfacial properties, device efficiency, and stability. The CN- and DIO-treated devices achieved maximum PCEs of 16.70% and 16.95%, surpassing the Control (15.05%). This was due to smoother morphology, reduced recombination losses, and enhanced charge carrier generation.

The DIO-treated device demonstrated superior stability, retaining 80% of its initial MPP for 745 min, compared to 431 min for CN-treated devices and 231 min for controls. This stability was linked to improved morphology and a higher dielectric constant that suppressed recombination. VIDAI also enhanced FF, short-circuit current ($J_{sc}$), and open-circuit voltage ($V_{oc}$) in both inverted and conventional structures. The promising results achieved with the bilayer system indicate that the VIDAI treatment could serve as an effective approach for improving the performance and stability of other OSCs by optimizing the interfaces between layers and electrodes. This simple and accessible method marks significant progress in advancing efficient and durable OSCs for practical use.

## 4 | Experimental Section

### 4.1 | Devices Fabrication

The ITO substrates were initially cleaned in a detergent and water bath with ultrasonic agitation for 1 h. Subsequently, in that

order, they underwent a 10 min ultrasonic cleaning process in ethanol, methanol, and isopropanol sequentially. Once cleaned, the ITOs were dried in an oven at 100°C for 10 min. Finally, the samples were exposed to UV–ozone treatment for 15 min to eliminate any residual organic impurities and enhance surface activation before the deposition of the ETL.

To deposit the ETL layer, the ZnO precursor solution was prepared by dissolving 150 mg of zinc acetate dihydrate in 1 mL of 2-methoxyethanol, followed by the addition of 30 μL of ethanolamine solution. The mixture was then vigorously stirred at 70°C for 1 h. To deposit the ZnO, we diluted the prepared solution by methanol with a volume ratio of 1:1 (v/v), then the diluted solution has been spin-coated on the cleaned ITO substrates at 4000 rpm for 45 s, followed by annealing at 200°C for 1 h in the open air.

For the donor layer D18, 4 mg of D18 powder was dissolved in 1 mL of chlorobenzene (CZ) and stirred continuously at 60°C for 3 h to ensure complete dissolution. The resulting D18 solution was then deposited onto the ZnO layer via dynamic spin coating at 2000 rpm for 40 s, ensuring uniform film formation.

For the CN-treated device, a 1-chloronaphthalene (CN) vapor was generated by heating a CN solution in a sealed glass Petri dish. The ITO/ZnO/D18 substrate was placed inside the sealed Petri dish for 10 min to allow vapor exposure. The same procedure was followed for the DIO-treated device, substituting 1-chloronaphthalene with 1,8-diiodooctane (DIO). For the Control device, the vapor treatment step was skipped.

We stabilized the vapor environment before treatment, limited exposure time to prevent condensation, and placed the samples under nitrogen for 1 h post-treatment to ensure a dry and clean donor surface.

Following the treatment step, the acceptor layer Y6 was prepared by dissolving 10 mg of Y6 powder in 1 mL of CF and stirring the mixture at 60°C for 3 h. The Y6 solution was then spin-coated onto the D18 layer at 2500rpm for 30 s. Finally, both layers underwent TA at 80°C for 5 min to optimize film morphology and device performance.

To deposit the HTL and the back electrode, we thermally evaporated 10 nm of $MoO_3$ powder followed by a 100 nm of Ag film which thermally evaporated under high vacuum $5 \times 10^{-7}$ mbar.

## 4.2 | Materials and Device Characterizations

Detailed information on the materials purchasing, preparation, and characterization techniques used for the devices in this study can be found in **Section S1** of the Supporting Information.

### Author Contributions

**Mohamed Samir**: data curation; formal analysis; investigation; methodology; validation; visualization; writing – original draft. **Osbel Almora**: data curation; formal analysis; investigation; review and editing. **Angel Sacramento**: formal analysis. **Josep Pallarès**: investigation; supervision; validation; review and editing. **Lluis F. Marsal**: conceptualization; formal analysis; funding acquisition; investigation; project administration; supervision; validation; writing – review and editing.


### Acknowledgments

M.S. acknowledges the financial support from Programa Martí i Franquès. O.A. and A.S thank the Ministry of Research and Universities, Department of Climate Action, Food and Rural Agenda and the Climate Fund of the Generalitat de Catalunya for funding the project Conversion of Energy in Sustainable Chemicals (CESC, 2023 CLIMA 00067). This work was further supported by the Spanish Ministerio de Ciencia e Innovación (MICINN/FEDER) under Grants PDI2021-128342OB-I00, by the Agency for Management of University and Research Grants (AGAUR) ref 2021-SGR-00739, and from the Catalan Institution for Research and Advanced Studies (ICREA) under the ICREA Academia Award.


### Conflicts of Interest

The authors declare no conflicts of interest.

### Data Availability Statement

The data that support the findings of this study are available on request from the corresponding author. The data are not publicly available due to privacy or ethical restrictions.

### References


1. D. Cevher, S. C. Cevher, and A. Cirpan, *Materials Today Communications* 37 (2023): 107524.

2. K. S. Santhoshi Kiran, V. Preethi, and S. Kumar, *Materials Today: Proceedings* 56 (2022): 3826.

3. Y. Zhang, Y. Lang, and G. Li, *EcoMat* 5 (2023): e12281.

4. Z. Fu, X. Zhang, H. Zhang, Y. Li, H. Zhou, and Y. Zhang, *Chinese Journal of Chemistry* 39 (2021): 381.

5. C. Liu, J. Liu, X. Duan, and Y. Sun, *Advanced Science* 10 (2023): 2303842.

6. X. Li, Q. Zhang, J. Yu, et al., *Nature Communications* 13 (2022): 2046.

7. Y. Xu, M. Xiao, Z. Fu, et al., *Advanced Functional Materials* 34 (2024): 2400810.

8. B. Sun, N. Tokmoldin, O. Alqahtani, et al., *Advanced Energy Materials* 13 (2023): 2300980.

9. T. N.-L. Phan, J.-W. Lee, E. S. Oh, *ACS Applied Materials & Interfaces* 14 (2022): 57070.

10. X. Li, R. Zhu, Z. He, et al., *ACS Applied Materials & Interfaces* 14 (2022): 25842.

11. X. Ma, Q. Jiang, W. Xu, et al., *Chemical Engineering Journal* 442 (2022): 136368.

12. S. Liu, Y. Zhou, Z. Liang, et al., *ACS Applied Energy Materials* 6 (2023): 5047.

13. D. Li, N. Deng, Y. Fu, et al., *Advanced Materials* 35 (2023): 2208211.

14. N. Chaturvedi, N. Gasparini, D. Corzo, et al., *Advanced Functional Materials* 31 (2021): 2009996.

15. Y. Li, H. Liu, J. Wu, et al., *ACS Applied Materials & Interfaces* 13 (2021): 10239.

16. R. Sorrentino, E. Kozma, S. Luzzati, and R. Po, *Energy & Environmental Science* 14 (2021): 180.

17. N. Ahmad, H. Zhou, P. Fan, and G. Liang, *Guangxing Liang* 4 (2022): e12156.

18. M. Jiang, H.-R. Bai, H.-F. Zhi, et al.,*ACS Energy Letters* 6 (2021): 2898.

19. C. Cui and Y. Li, *Aggregate* 2 (2021): e31.

20. C. Guo, D. Li, L. Wang, et al., *Advanced Energy Materials* 11 (2021): 2102000.

21. Y. Zheng, S. Li, D. Zheng, and J. Yu, *Organic Electronics* 15 (2014): 2647.

22. L. Zhang, J. Zhang, Y. Ma, et al., *Organic Electronics* 130 (2024): 107075.

23. K. Jiang, J. Zhang, Z. Peng, et al., *Nature Communications* 12 (2021): 468.

24. Y. Song, K. Zhang, S. Dong, R. Xia, F. Huang, and Y. Cao, *ACS Applied Materials & Interfaces* 12 (2020): 18473.

25. A. Mishra, N. N. Bhuyan, H. Xu, and G. D. Sharma, *Materials Advances* 4 (2023): 6031.

26. L. Lu, T. Zheng, Q. Wu, A. M. Schneider, D. Zhao, and L. Yu, *Chemical Reviews* 115 (2015): 12666.

27. S. Mahdy, M. Feteha, M. Soliman, H. Hussien, T. Sadat-Shafai, and S. Ebrahim, *Journal of Materials Science* 58 (2023): 17543.

28. S. Karuthedath, Y. Firdaus, A. D. Scaccabarozzi, et al., *Small Structures* 3 (2022): 2100199.

29. A. Zusan, M. Zerson Börn Gieseking, V. Dyakonov, R. Magerle, and C. Deibel, *Scientific Reports* 5 (2015): 8286.

30. S. Kwon, J. K. Park, J. Kim, et al., *Journal of Materials Chemistry A* 3 (2015): 7719.

31. S. Xiong, Y. Zhu, Y. Wang, et al., *ACS Applied Materials & Interfaces* 17 (2025): 18473.

32. T.-C. Wu, Y.-S. Long, S.-T. Hsu, and E.-Y. Wang, *Energy Procedia*.130 (2017): 66.

33. B. H. Hamadani, Y. S. Long, M. A. Tsai, and T. C. Wu, *IEEE Journal of Photovoltaics* 11 (2021): 1430.

34. O. Almora, K. T. Cho, S. Aghazada, et al., *Nano Energy* 48 (2018): 63.

35. E. Moustafa, M. Méndez, J. G. Sánchez, J. Pallarès, E. Palomares, and L. F. Marsal, *Advanced Energy Materials* 13 (2023): 2203241.

36. X. Xia, L. Mei, C. He, et al., *Journal of Materials Chemistry A* 11 (2023): 21895.

37. Y.-C. Huang, G. C. Welch, G. C. Bazan, M. L. Chabinyc, and W.-F. Su, *Chemical Communications* 48 (2012): 7250.

38. V. D. Mihailetchi, L. J. A. Koster, J. C. Hummelen, and P. W. M. Blom, *Physical Review Letters* 93 (2004): 216601.

39. M. Samir, E. Moustafa, O. Almora, et al., *ACS Applied Materials & Interfaces* 16 (2024): 16317.

40. Z. Liu and N. Wang, *Journal of Materials Chemistry C* 7 (2019): 10039.

41. B.-H. Jiang, Y.-P. Wang, C.-Y. Liao, et al., *ACS Applied Materials & Interfaces* 13 (2021): 1076.

42. V. Gupta, A. K. K. Kyaw, D. H. Wang, S. Chand, G. C. Bazan, and A. J. Heeger, *Scientific Reports* 3 (2013): 1965.

43. P. Hartnagel and T. Kirchartz, *Advanced Theory and Simulations* 3 (2020): 2000116.

44. O. Almora, C. I. Cabrera, J. Garcia-Cerrillo, T. Kirchartz, U. Rau, and C. J. Brabec, *Advanced Energy Materials* 11 (2021): 2100022.

45. A. Zeng, X. Ma, and M. Pan et al., *Advanced Functional Materials* 31 (2021): 2102413.

46. Y. Zhang, X. Li, T. Dai, et al., *The Journal of Physical Chemistry C* 123 (2019): 24446.

47. S. Benramache, Y. Aoun, S. Lakel, B. Benhaoua, and C. Torchi, *Sādhanā* 44 (2019): 26.

48. H. F. Haneef, A. M. Zeidell, and O. D. Jurchescu, *Journal of Materials Chemistry C* 8 (2020): 759.

49. F. Urbach, *Physical Review* 92 (1953): 1324.

50. S. Liu, J. Yuan, W. Deng, et al., *Nature Photonics* 14 (2020): 300.

51. A. Pockett, H. K. H. Lee, B. L. Coles, W. C. Tsoi, and M. J. Carnie, *Nanoscale* 11 (2019): 10872.

52. E. Osorio, J. G. Sánchez, L. N. Acquaroli, et al., *ACS Omega* 2 (2017): 3091.

53. E. von Hauff, *The Journal of Physical Chemistry C* 123 (2019): 11329.

54. L. Contreras-Bernal, S. Ramos-Terrón, A. Riquelme, et al., *Journal of Materials Chemistry A* 7 (2019): 12191.

55. O. Almora, J. Wiegand, P. López-Varo, G. J. Matt, and C. J. Brabec, *Solar RRL* 5 (2021): 2100024.

56. T. Kirchartz, W. Gong, S. A. Hawks, et al., *The Journal of Physical Chemistry C* 116 (2012): 7672.

57. F. Wang, M. Yang, Y. Zhang, et al., *Nano Research* 14 (2021): 2783.

58. M. B. Upama, N. K. Elumalai, M. A. Mahmud, et al.,*Solar Energy Materials and Solar Cells* 176 (2018): 109.

59. S. Günes, H. Neugebauer, and N. S. Sariciftci, *Chemical Reviews* 107 (2007): 1324.

60. W. Gao, R. Ma, T. A. Dela Peña, et al., *Nature Communications* 15 (2024): 1946.

61. Y. Li, X. Huang, K. Ding, et al., *Nature Communications* 12 (2021): 5419.

62. A. Foertig, J. Kniepert, M. Gluecker, et al., *Advanced Functional Materials* 24 (2014): 1306.

63. R. Ma, Y. Tao, Y. Chen, et al., *Science China Chemistry* 64 (2021): 581.

64. O. Almora, G. C. Bazan, C. I. Cabrera, et al., *Advanced Energy Materials* n/a (2024): 2404386.

65. J. Oh, S. Jung, M. Jeong, et al., *Journal of Materials Chemistry C* 7 (2019): 4716.

66. R. Su, Z. Xu, J. Wu, et al., *Nature Communications* 12 (2021): 2479.

67. A. Sacramento, M. Ramírez-Como, V. S. Balderrama, et al., *Journal of Materials Chemistry C* 9 (2021): 6518.

## Supporting Information

Additional supporting information can be found online in the Supporting Information section.